Acta Mech 236, 3211–3229 (2025)
https://doi.org/10.1007/s00707-025-04321-w

ORIGINAL PAPER

D. Maraglino · D. De Padova · M. Mossa · F. Zonta · A. Soldati

Large eddy simulation of a turbulent submerged jet interacting with a wave environment

Received: 19 February 2025 / Revised: 10 March 2025 / Accepted: 12 March 2025 / Published online: 9 April 2025

Abstract We use numerical simulations to study the interaction between a turbulent jet, discharged vertically from a circular nozzle at the bottom of a horizontal liquid layer of height $h_0 = 0.35$ m, and surface waves. All simulations are run at a fixed value of the jet Reynolds number ($\mathrm{Re}_j = 20{,}000$, based on the nozzle diameter) and for two different values of the surface waves elevation, $H = 0.02$ m (simulation $R1$) and $H = 0.03$ m (simulation $R2$). A reference simulation, assuming a free surface without waves, is also performed for comparison purposes (simulation $R0$). We focus on the influence of the surface waves on the jet flow field, considering in particular the behavior of the jet width and of the mean jet velocity—which we analyze applying a phase-averaged technique. Our results show that surface waves induce a reduction of the vertical component of the jet velocity, and a corresponding increase of the horizontal components of the jet velocity. In particular, we observe that the reduction of the centerline mean vertical velocity (along the vertical direction z) is linear in the region close to the jet nozzle, $W_0/W_m \sim z$, but can be faster than linear (superlinear) in the region close to the liquid surface, for the larger amplitude waves. Correspondingly, the jet width increases linearly with z, $b \sim C\,(z/d_0)$, but at a slope C that does depend on the distance from the liquid surface. These findings suggest that surface waves enhance entrainment and dilution, offering insights for improving jet–wave interaction models and parameterizations.

1 Introduction

Understanding how pollutants disperse in the marine environment, through both models [1,2] and experimental methods [3], is essential for managing environmental impacts. Submerged jets are key in processes such as discharging wastewater, stormwater, and runoff into the ocean. These jets promote mixing and dilution, helping to reduce the harmful effects of pollutants by dispersing them throughout the surrounding water [2,4,5]. Due to its important applications, the literature on the field of submerged jets is vast, but is mainly focused on the case of submerged jets in stagnant environments [6–13]. However, terrestrial water bodies and oceans are often

D. Maraglino · D. De Padova (✉) · M. Mossa
Department of Civil, Environmental, Land, Building Engineering and Chemistry,
Polytechnic University of Bari, Bari, Italy
E-mail: diana.depadova@poliba.it

D. Maraglino · A. Soldati
Institute of Fluid Mechanics and Heat Transfer, Technical University of Vienna, Vienna, Austria

F. Zonta
School of Engineering, Newcastle University, Newcastle upon Tyne NE17RU, UK

A. Soldati
Polytechnic Department, University of Udine, Udine, Italy

characterized by wave-induced currents and oscillations, which have characteristic time scales of the same order of magnitude compared to those of turbulent jets [14], making the study of jet–current interactions of great practical importance.

The first study of a jet issued in a wave environment was carried out by Shuto and Ti [15], who observed that the dilution rate (measured based on the concentration of chromium near the water surface) of a horizontal buoyant jet in standing waves was significantly enhanced by the wave motion. Similar results were also obtained by Ger [16], who attributed the improved dilution rate to the oscillation of the jet trajectory. Naturally, the influence of wave-induced currents on the jet dynamics depends on the depth of the liquid layer in which the jet is issued. This aspect was analyzed by Sharp [17], looking at flow visualizations of a jet issued in a deep water and shallow water wave environment. In deep water conditions, the jet was found to be almost unaffected by the wave field in the bottom third of the water depth, an observation that was primarily attributed to the exponential damping of orbital motion. In the upper two-thirds of the water depth, the orbital motions induced by the waves were found to enhance the spread of the jet. In shallow water conditions and because of the almost negligible damping of orbital motions with depth, a significant spread of the submerged jet was observed over the entire depth of the water layer. Another important aspect of the problem, already considered in the archival literature [18–20], is represented by the orientation of the jet, which can change from horizontal to vertical. Relevant to the present work is the observation that vertically oriented jets induce higher dilution rates compared to horizontal ones [21].

Although the dynamics of jets in a wave environment depends on a number of parameters, like jet size, jet velocity, but also wave amplitude, steepness and frequency, it would be desirable to identify a single parameter to characterize the problem. A first attempt in this direction was done by Mori and Chang [22], who identified—as main parameter—the wave-to-jet momentum ratio

$$R_m = \frac{g a^2}{2 d W_0^2}, \tag{1}$$

with a the wave amplitude, d the diameter of the nozzle, W_0 the discharged velocity, and g the acceleration due to gravity. Based on the value of R_m, Mori and Chang [22] classified the behavior of the jet flow into three categories. For values of R_m less than 0.05, a symmetric jet motion is observed (Type I behavior). For $0.05 < R_m < 0.2$, the jet motion becomes asymmetric (Type II behavior). For $R_m > 0.2$, the jet motion is asymmetric and the jet centerline discontinuous (Type III behavior).

However, R_m alone is not sufficient to predict, for example, the centerline axial velocity decay. For this reason, Fang et al. [23] (later followed by Anghan et al. [24]) introduced an additional parameter, the ratio of the jet inlet velocity to the wave orbital motion:

$$R_{jw} = \frac{W_0}{\frac{\pi H \cosh(k h_0)}{\mathcal{T} \sinh(k h)}} \tag{2}$$

where h_0 is the vertical distance between the nozzle outlet and the bottom of the fluid layer, h is the depth of the water layer, $\mathcal{T}$ is the wave period and H the wave height. For very high values of R_{jw}, typically over 100, the behavior of the jet is similar to that of a free jet; otherwise, the rate of decay of the centerline axial velocity is larger for decreasing R_{jw}. Note indeed that an high value of R_{jw} indicates that the effects of wave momentum are smaller compared to the jet momentum, and for $R_{jw} > 100$ the wave momentum becomes negligible. Given the inherent difficulties associated with the design and realization of accurate experiments of jet–wave interactions, numerical simulations have emerged as a valuable tool of analysis [9,25–31]. In a series of previous works [27,28], we studied the problem of jet–wave interactions via 2D Smoothed Particle Hydrodynamics (SPH), and we showed that the jet can be significantly influenced by surface waves even at small distance from the jet nozzle (i.e., at distances of the order of $10d$ from the nozzle, with d the nozzle diameter). In addition, the wave period was found to influence more the free surface region than the interior region of the flow. In the present study, we make a step forward, and we analyze the jet–wave interactions via 3D Large Eddy Simulation (LES), an approach which is expected to represent closely the flow phenomenology we wish to highlight. In a 3D setting, the vorticity dynamics is dominated by the vortex stretching term, $\omega \cdot \nabla u$ (with ω the vorticity and ∇u the velocity gradient tensor), which is identically equal to zero in 2D. Note that, as also discussed in detail by [24], a precise characterization of the 3D turbulent flow is crucial to capture the small-scale dynamics of the flow and hence the mixing process and the corresponding dilution rate. Without resolving the small-scale flow structures, key phenomena such as the wave-induced oscillatory motion or the jet entrainment cannot be accurately captured, potentially leading to an incomplete or incorrect prediction of the

jet behavior under realistic conditions. As apparent from the previous literature review, the current study can provide reliable reference results on the dynamics of vertical, submerged turbulent jets interacting with waves, since most of the previous studies were constrained to two-dimensional (2D) settings, with few remarkable exceptions appeared only recently (see for example Anghan et al. [21]). The aim of this study is therefore to provide a characterization of the flow field induced by the interaction between a vertical submerged jet and mechanically generated surface waves in a three-dimensional configuration.

2 Numerical method

2.1 Numerical methods

With reference to the schematics of Fig. 1, we consider a submerged jet that interacts with waves propagating at the surface of a horizontal liquid layer. The jet is issued from a circular nozzle of diameter $d = 0.02$ m—located at the center of the bottom plate—and flows vertically toward the top deformable surface, where waves can also be generated. The liquid layer has dimensions $200d \times 50d \times 17.5d$, along the $x = x_1$, $y = x_2$ and $z = x_3$ directions, respectively (z indicating the vertical direction). This corresponds to a domain of size 4 m $\times$1 m $\times$0.35 m. Accordingly, the velocity components are $u_1 = u$ (horizontal velocity component, positive if oriented in the same direction of the waves propagation), $u_2 = v$ (spanwise velocity component, in the direction y) and $u_3 = w$ (vertical velocity component, positive if oriented upwards). The problem is solved numerically performing large eddy simulations (LES) with the OpenFOAM solver, and accounting for the waves propagation at the liquid surface via the module *potentialFreeSurfaceFoam* (PSFS, for ease of reading), by which—solving for the wave height field—single-phase simulations of a deformable surface can be performed. The PSFS solver adds a source term $r_w A_{wm}$ for wave generation, where r_w is a binary scalar that defines the wavemaker region ($r_w = 1$) and A_{wm} is the acceleration input to the wavemaker, and a sink term ($Sn_z U$) mimicking a numerical beach and acting in the vertical direction [32]. This solver can predict the behavior of a free surface if the effect of air can be neglected, and if waves do not break. The computational cost of PFSF is significantly lower than that of interface-capturing solvers (for example of the volume-of-fluid method, VOF). The interesting thing of PFSF is that it does not explicitly solve for a free surface that continuously deforms in time and space (a circumstance that would require a mapping procedure between the computational and the physical domain). The effect of the free surface is simulated via specific boundary conditions (*waveSurfacePressure*). The problem is therefore solved on a fixed grid, and the deformation of the free surface is translated into a wave height and a corresponding pressure change due the change of the free surface profile. Note that the change in the free surface profile is obtained upon integration of the fluid velocity at the free surface over time, while the pressure change induced by the variation of the free surface position η with respect to the equilibrium case (flat, horizontal, surface) is obtained as $\Delta p = g\eta$. Further details and benchmarks on the solver can be found in [32].

Within the LES framework (which is based on filtering Navier–Stokes equations in space), and indicating with the symbol $\widehat{\ }$ the filtering operation, the governing equations read as:

$$\frac{\partial \widehat{u}_i}{\partial x_i} = 0 \tag{3}$$

$$\frac{\partial \rho \widehat{u}_i}{\partial t} + \frac{\partial \rho \widehat{u}_i \widehat{u}_j}{\partial x_j} = -\frac{\partial \widehat{p}}{\partial x_i} + \rho g_i + \mu \frac{\partial^2 \widehat{u}_i}{\partial x_j \partial x_j} - \frac{\partial \tau_{ij}}{\partial x_j} \tag{4}$$

where $\widehat{u}_i$ is the i-th filtered component of the velocity vector, g_i is the i-th component of the gravitational acceleration vector, $\widehat{p}$ is the filtered pressure, μ is the dynamic viscosity, ρ is density, and τ_{ij} is the subgrid stress (SGS) defined as:

$$\tau_{ij} = \rho \widehat{u_i u_j} - \rho \widehat{u}_i \widehat{u}_j \tag{5}$$

and calculated as follows:

$$\tau_{ij} - \frac{1}{3}\tau_{kk}\delta_{ij} = -2\mu_t \widehat{S}_{ij}, \tag{6}$$

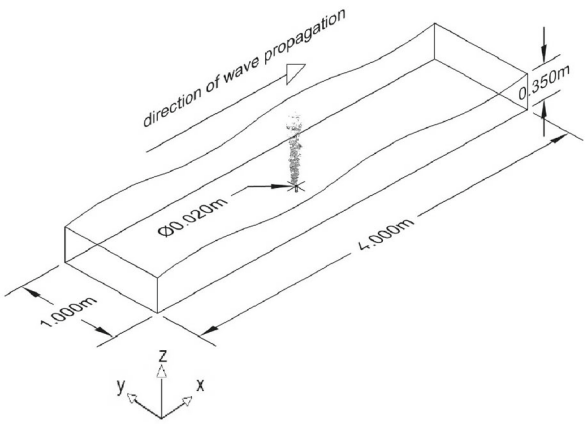

(a) Computational domain.

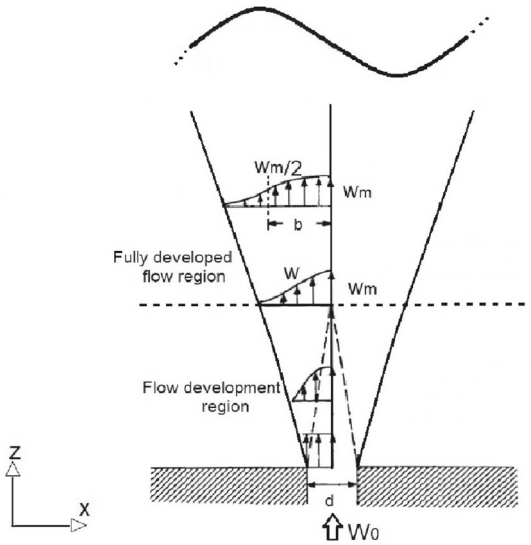

(b) Sketch of the jet, with the indication of the main flow parameters: d is the diameter of the nozzle, W is the vertical velocity of the jet (and W_m its value at the jet axis and W_0 the discharge velocity), b is the jet width.

Fig. 1 Computational domain (**a**) and sketch of the jet (**b**)

where μ_t is the eddy viscosity (computed in the framework of the dynamic SGS model), τ_{kk} is the isotropic part of the SGS, δ_{ij} is the Kronecker delta and $\hat{S}_{ij}$ is the rate of strain tensor for the filtered field,

$$\widehat{S}_{ij} = \frac{1}{2}\left(\frac{\partial \widehat{u}_i}{\partial x_j} + \frac{\partial \widehat{u}_j}{\partial x_i}\right). \tag{7}$$

In the present study, we used the dynamic kinetic energy SGS model [33], in which the eddy viscosity μ_t is defined as $\mu_t = c_v\sqrt{k_{SGS}}\Delta$, with Δ the filter size (computed as $V^{1/3}$, with V the volume of the computational cell) and $k_{SGS} = \frac{1}{2}\left(\widehat{u_k^2} - \widehat{u_k}^2\right)$ the subgrid scale kinetic energy. The behavior of k_{SGS} is obtained by solving a transport equation in which the model constants are dynamically determined (see [33] for further details).

Time integration of the governing equations is realized via a second-order backward scheme, while space integration is realized via a second-order linear interpolation scheme. The timestep is dynamically adjusted so to keep the Courant number smaller than 0.5.

Table 1 Summary of the main parameters of the simulations

Run	Jet velocity W_0 (m/s)	Re_j	Wave period $\mathcal{T}$ (s)	Wave height H (cm)	Wavelength λ (m)	$\frac{2\pi h}{\lambda}$	R_m	R_{jw}
$R0$	1	2×10^4	–	–	–	–	–	–
$R1$	1	2×10^4	1	2	1.47	1.496	0.025	33.74
$R2$	1	2×10^4	1	3	1.47	1.496	0.055	22.49

We consider three different cases, which we label $R0$, $R1$ and $R2$ (see Table 1). Each case is characterized by the same value of the jet inlet velocity ($W_0 = 1$ m/s) and diameter ($d = 0.02$ m) and hence of the jet Reynolds number Re_j, but different conditions at the free surface. In particular, in $R0$ we consider a jet submerged in a stagnant liquid layer. In $R1$ and $R2$, regular waves are generated at the free surface, with wave period $\mathcal{T} = 1$s, wave length $\lambda = 1.47$ m and wave height $H = 0.02$ m ($R1$) and $H = 0.03$ m ($R2$). A summary of the main parameters of the simulations is provided in Table 1. In particular, k is the wave number of the imposed surface deformation (when it is undisturbed by the jet), defined as $k = \frac{2\pi}{\lambda}$. For each simulation in the presence of waves, $kh = 1.496 < \pi$, the analysis was carried out in shallow (or transition) water conditions. The value of the wave to jet momentum ratio R_m and of the ratio of the jet inlet velocity to the wave orbital motion R_{jw} is also given.

The mesh resolution is finer near the jet inlet and in the region above the jet nozzle (truncated-cone refinement region, with minor base diameter of 0.0250 m and major base diameter of 0.12 m, mimicking the jet shape), with the minimum grid size of $3.125 \cdot 10^{-4}$ m and the maximum grid size of $5 \cdot 10^{-3}$ m, for on overall of about 65 million non-uniform cells. Details on the mesh sensitivity analysis performed to evaluate the suitable mesh resolution are given in Appendix A. Uniform inlet velocity condition is enforced at the jet nozzle, while a total pressure condition is imposed at the outlet. A wall boundary condition is applied at all other boundaries but at the free surface, where the condition provided by the wave solver has been prescribed.

2.2 Model validation

Given the relatively small number of studies focused on submerged jets interacting with a deformable surface, we decided to validate our numerical results against previous data on free jets. In Fig. 2, time-averaged profiles of the vertical velocity W are shown for the case $R0$ (i.e., submerged jet in stagnant environment). The velocity field is averaged over a time-window $\Delta T = 10\tau_j$, where $\tau_j = r_j / W_0 = 0.01$s is the characteristic timescale of the jet. Results of the mean velocity, which are normalized by the value W_m of the velocity observed at the jet axis, are shown as a function of the normalized distance from the jet axis x/b, with b the jet width (defined as the radial distance from the axis at which the value of the time-averaged vertical velocity is half the size of that of the velocity at the axis). Results are evaluated at three different distances z, measured from the jet nozzle: $z/d = 8$, $z/d = 10$ and $z/d = 12$.

The mean velocity profiles for a turbulent-free round jet from Tollmien [34] and Goertler [35] can be used for comparison purposes with the present results, as shown in Fig. 2. To evaluate the accuracy of the results, a comparison between the numerical and the theoretical results in terms of the Wilmott index [36] has been carried out:

$$Iw = 1 - \frac{\sum_{k=1}^{N} (x_{ck} - x_{mk})^2}{\sum_{k=1}^{N} [|x_{ck} - \overline{x_m}| + |x_{mk} - \overline{x_m}|]^2} \tag{8}$$

where x_c and x_m are the theoretical and numerical values of the variable x, respectively, while the overbar indicates time-averaged quantities. Values of Iw close to one indicate a very good agreement between theoretical and numerical results. As can be observed from both Fig. 2 and Table 2, the agreement between reference theoretical data and current results is nice. In particular, as already pointed out by Rajaratnam [10], we note that the Goertler solution [35] seems to approximate better the numerical results near the axis of jet (for $x/b < 1$), while the Tollmien solution [34] seems to approximate better the numerical results in the shear-layer/outer regions ($x/b > 1.2$).

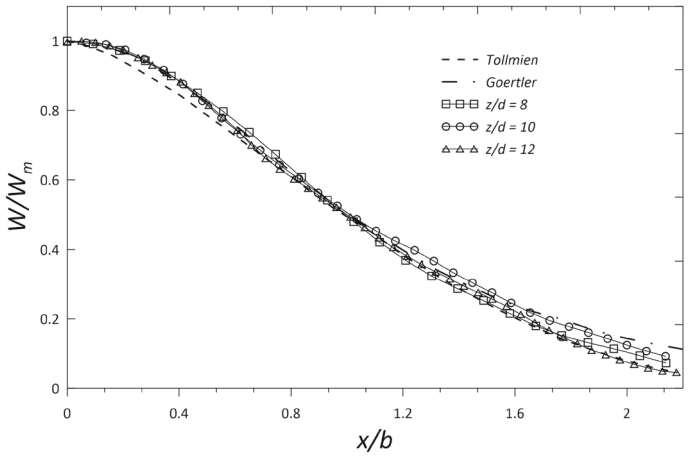

Fig. 2 Behavior of the normalized mean vertical velocity of the jet, W/W_m, as a function of the radial distance from the jet axis x/b. Results of the numerical simulations (symbols) are evaluated at three different vertical locations (distance from the jet nozzle): $z/d = 8$, $z/d = 10$ and $z/d = 12$. The Tollmien [34] and Goertler [35] solutions valid for free jets are also included (dashed and dot-dashed lines) for comparison purposes

Table 2 Wilmott index for Tollmien and Goertler curves

z/d	Iw $R0$—Tollmien	Iw $R0$—Goertler
8	0.9990	0.9984
10	0.9981	0.9992
12	0.9992	0.9979

3 Results

In the following sections, the mutual interaction between the surface waves and the submerged jet is considered. We look first at the influence of the surface waves on the jet behavior and then at the influence of the jet on the propagation of surface waves.

3.1 Velocity decomposition

Waves are organized coherent motions. To separate the effects of these organized motions from the turbulent flow field and to clarify the role of waves on the jet dynamics, the flow velocity is decomposed as follows [37]:

$$u_i\left(x_i,t\right)=\langle u_i\rangle\left(x_i,t\right)+u_i'\left(x_i,t\right)=U_i\left(x_i\right)+\tilde{u}_i\left(x_i,t\right)+u_i'\left(x_i,t\right) \tag{9}$$

where the angular brackets indicate ensemble (or phase) average, the tilde indicates the fluctuations due to the coherent motion of waves, the prime symbol indicates the turbulent fluctuations, while the overbar or, for ease of notation, the capital letter (see also Eq. 11), indicates time-averaged quantities. Considering a Cartesian reference frame (as represented also in Fig. 1), the coordinates $x_i (i = 1, 2, 3; x_1 = x, x_2 = y, x_3 = z)$ define the streamwise (i.e., direction of the waves propagation), the spanwise, and the vertical (i.e., aligned with the jet axis) directions, respectively. Therefore, the velocity components are: $u_1 = u$, the horizontal velocity component (positive if oriented in the same direction of the waves propagation); $u_2 = v$, the velocity component in the spanwise direction y; $u_3 = w$, the vertical velocity component (positive if oriented upward). The ensemble average of the equations of motion for a turbulent jet flow in the presence of waves gives:

$$\frac{\partial\langle u_i\rangle}{\partial t}+\frac{\partial\langle u_i\rangle\langle u_j\rangle}{\partial x_j}=\frac{1}{\rho}\frac{\partial}{\partial x_j}\left(-\langle p\rangle\delta_{ij}+\mu\left(\frac{\partial\langle u_i\rangle}{\partial x_j}+\frac{\partial\langle u_j\rangle}{\partial x_i}\right)-\rho\langle u_i'u_j'\rangle\right). \tag{10}$$

We remark that, given two generic components $u_i(t)$ and $u_j(t)$ of the velocity field, and—as mentioned above—indicating with overbars the time averaged quantities, the following properties hold:

$$\begin{aligned} &\langle u_i' \rangle = 0; \qquad \overline{\tilde{u}_i} = 0; \qquad \overline{u_i'} = 0; \qquad \overline{\langle u_i \rangle} = \langle \overline{u}_i \rangle = U_i; \\ &\langle \tilde{u}_i u_j \rangle = \tilde{u}_i \langle u_j \rangle; \qquad \langle \overline{u}_i u_j \rangle = U_i \langle u_j \rangle; \qquad \overline{\langle \tilde{u}_i u_j' \rangle} = \overline{\tilde{u}_i u_j'} = 0. \end{aligned} \tag{11}$$

Since the flow is periodic along x and y, Eq. 10 becomes:

$$\frac{\partial}{\partial x_j}\left(U_i U_j + \overline{\tilde{u}_i \tilde{u}_j} + \overline{u_i' u_j'}\right) = \frac{1}{\rho}\left(-\frac{\partial P}{\partial x_j}\delta_{ij} + \mu \frac{\partial^2 U_i}{\partial x_j \partial x_j}\right) \tag{12}$$

3.2 Oscillating velocity components

In the literature, turbulent velocity components of jets in the presence of surface waves are often obtained subtracting the velocity components calculated using Airy's theory from the directly measured velocity components. To evaluate the robustness of this approach, in Figs. 3 and 4 we compare the velocity components computed from Airy's theory (dash-dotted line) with those obtained by phase averaging the velocity field (dashed line). Results show the time series of wave elevation profile η and vertical oscillating velocity components $\tilde{w}$ evaluated at the jet axis ($x = 0$ m, panels a,c) and outside the jet axis ($x = 0.1$ m, panels b,d) at two different distances from the jet nozzle, i.e., $z/d = 12.5$ (panels a,b) and $z/d = 15$ (panels c,d). Figure 3 refers to simulation $R1$, while Fig. 4 refers to simulation $R2$ (see Table 1). Confirming previous experimental results [38], high velocity values are observed under the wave trough along the jet centerline and far from the wavy surface. This happens because the wave pressure variation at the nozzle reaches its maximum under the wave crest, and its minimum under the wave trough. As a consequence, the wave elevation and the discharge velocity are out of phase by π. When we move closer to the wavy surface, the mutual interaction between the jet and the surface is stronger and more complex to model. Farther away from the jet axis ($x = 0.1$ m), the wave elevation profile and the discharge velocity are $\pi/2$ out of phase. This is attributed to the stronger influence of wave motion in that region. Current results also show an important aspect: the oscillating vertical velocity components (in particular at the jet centerline, no matter the distance from the surface) present maxima that are larger than those obtained from the classic wave motion theories (dashed lines). This difference gradually disappears as we move off the jet axis, where the numerical and theoretical phase-averaged velocities start to match.

3.3 Mean jet velocity

The behavior of the mean jet velocity is shown in Fig. 5. In particular, Fig. 5a, c, e refers to the mean vertical velocity W at three different vertical locations ($z/d = 10$ for Fig. 5a, $z/d = 12.5$ for Fig. 5c, $z/d = 15$ for Fig. 5e), while Fig. 5b, d, f refers to the mean horizontal velocity U (monitored at the same three different vertical locations, i.e., $z/d = 10$ for Fig. 5b, $z/d = 12.5$ for Fig. 5d, $z/d = 15$ for Fig. 5f). In each panel, the results of the simulations with prescribed wave heights $H = 0.02$ m and $H = 0.03$ m—labeled $R1$ and $R2$, respectively—are compared with the results of the simulation with a free surface (labeled $R0$). Looking at the behavior of the vertical jet velocity (Fig. 5a, c, e), we immediately notice that, compared to the case of the free surface, the profile of W decreases in magnitude and becomes broader for a wavy water surface. The reduction of the vertical velocity magnitude, along with a corresponding broadening of the profile in the lateral direction, is due to the entrainment effect: to preserve the jet momentum, entrainment of quiescent fluid by the jet (i.e., increase in mass moving vertically) must be associated with a reduction of the mean vertical velocity magnitude. From the comparison between the results of $R0$, $R1$ and $R2$, we observe that a higher entrainment is observed for higher wave heights. This is due to the presence, in addition to the classical entrainment, of other mechanisms, for example, jet deflection and wave tractive mechanisms, which contribute to a more efficient mixing of the jet with the surrounding fresh water [18].

Previous observations are confirmed by the behavior of the mean horizontal velocity U, see Fig. 5b, d, f. Not surprisingly, we notice the presence—in the mean horizontal velocity profile—of an inward flow that brings fluid from outside to the jet axis (this is identified by $U < 0$ for $x > 0$, and by $U > 0$ for $x < 0$). The profiles of U are qualitatively similar, regardless of the vertical position z at which they are calculated, with perhaps only minor differences observed very close to the wavy surface ($z = 0.3$ m, in Fig. 5). Further turbulence statistics are presented in Appendix B.

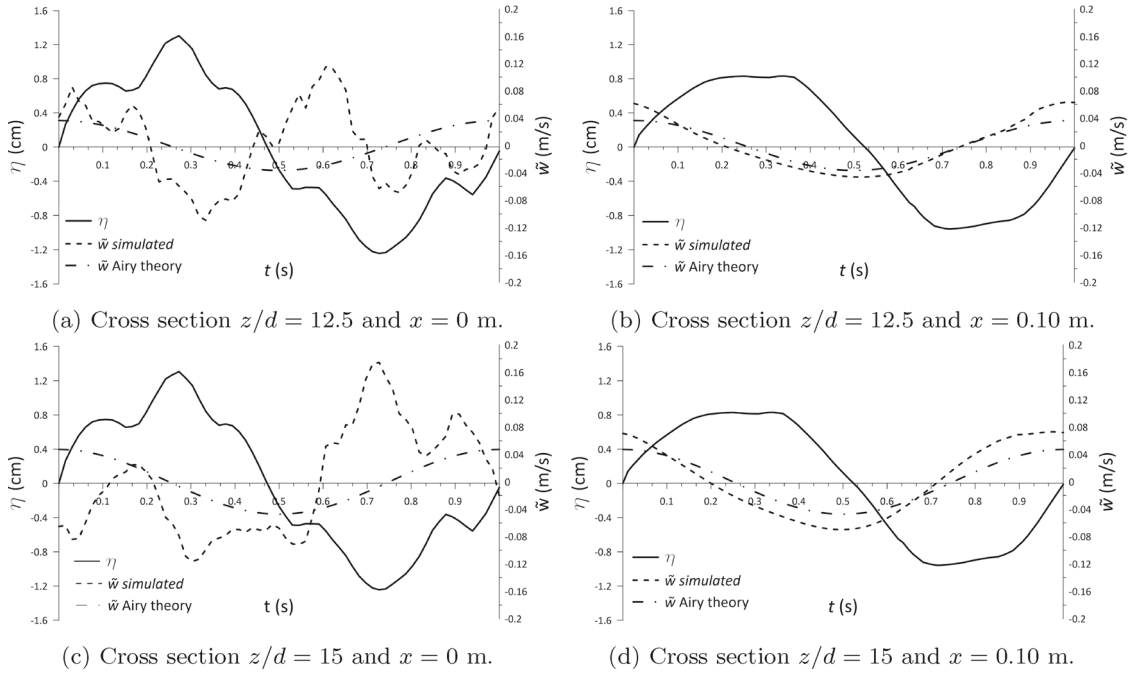

(a) Cross section $z/d = 12.5$ and $x = 0$ m. (b) Cross section $z/d = 12.5$ and $x = 0.10$ m.

(c) Cross section $z/d = 15$ and $x = 0$ m. (d) Cross section $z/d = 15$ and $x = 0.10$ m.

Fig. 3 Wave elevation profile (η) and oscillating vertical velocity component ($\tilde{w}$) over a wave period evaluated at two different distances from the jet nozzle (12.5 and 15) along the jet axis ($x = 0$ m) and outside the jet axis ($x = 0.1$ m) m for simulation $R1$ (see Table 1). The behavior of the vertical velocity component as predicted by the Airy theory (dash-dotted line) is also shown for comparison

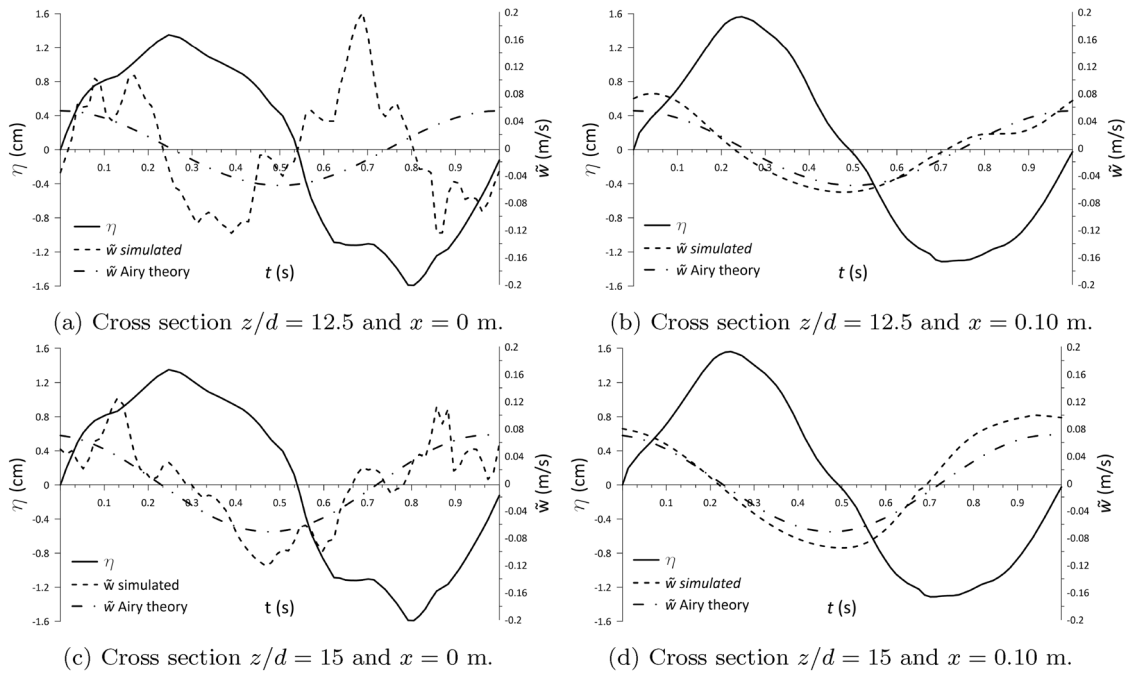

(a) Cross section $z/d = 12.5$ and $x = 0$ m. (b) Cross section $z/d = 12.5$ and $x = 0.10$ m.

(c) Cross section $z/d = 15$ and $x = 0$ m. (d) Cross section $z/d = 15$ and $x = 0.10$ m.

Fig. 4 Wave elevation profile (η) and oscillating vertical velocity component ($\tilde{w}$) over a wave period evaluated at two different distances from the jet nozzle (12.5 and 15) along the jet axis ($x = 0$ m) and outside the jet axis ($x = 0.1$ m) m for simulation $R2$ (see Table 1). The behavior of the vertical velocity component as predicted by the Airy theory (dash-dotted line) is also shown for comparison

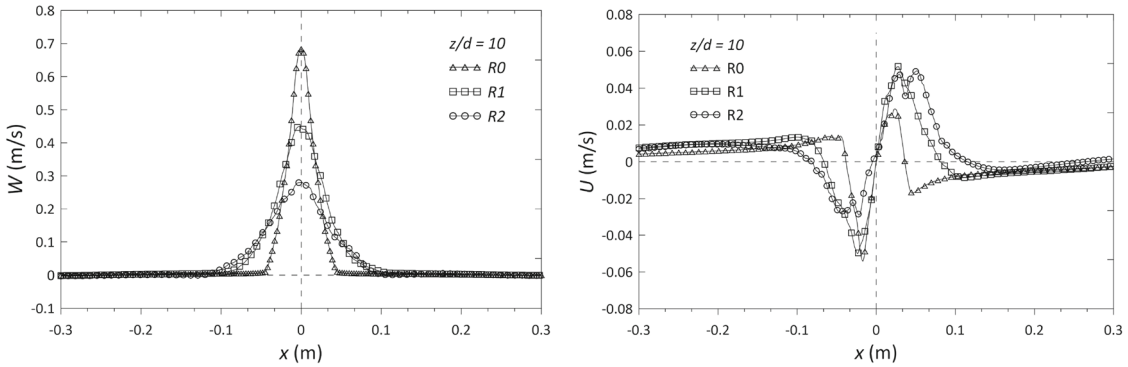

(a) Cross section z/d=10. Vertical component. (b) Cross section z=10. Horizontal component.

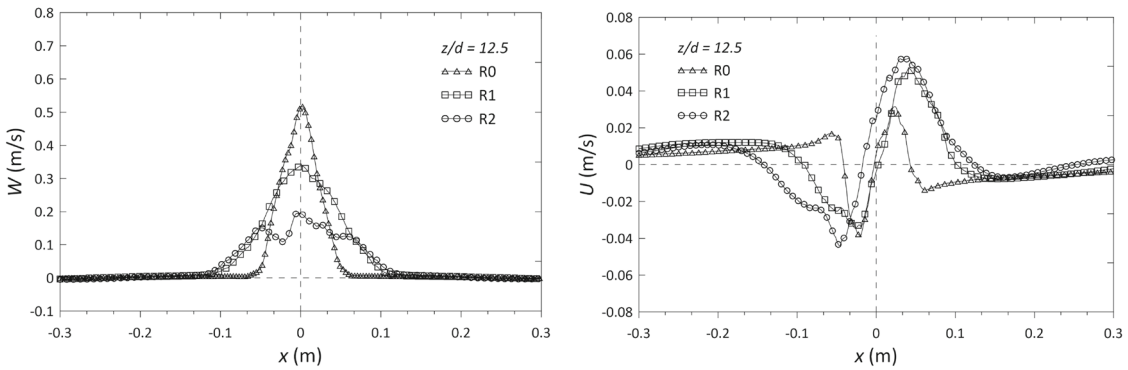

(c) Cross section z/d=12.5. Vertical component. (d) Cross section z/d=12.5. Horizontal component.

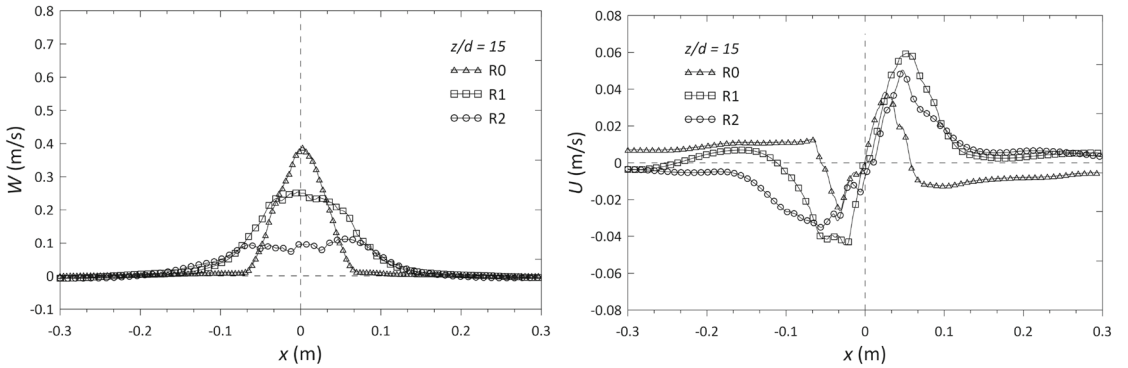

(e) Cross section z/d=15. Vertical component. (f) Cross section z/d=15. Horizontal component.

Fig. 5 Behavior of the vertical (panels **a**, **c**, **e**) and horizontal (panels **b**, **d**, **f**) components of the jet velocity at three different locations, measured from the jet nozzle ($z/d = 10$, panels **a**, **b** $z/d = 12.5$, panels **c**, **d** $z/d = 15$, panels **e**, **f**). Results obtained from all three simulations, $R0$, $R1$ and $R2$, are compared

3.4 Centerline axial velocity decay and variation of jet width

As already anticipated in the previous sections, the development of the jet along the vertical (z) direction is influenced by the entrainment of the quiescent fluid, which induces the spreading (broadening) of the jet in the transversal direction (x), and—from momentum conservation—a corresponding reduction in the magnitude of the vertical velocity.

The centerline velocity w_m of the circular turbulent jet can be expressed as [10]:

$$w_m = f_1\,(M_0, \rho, z)$$

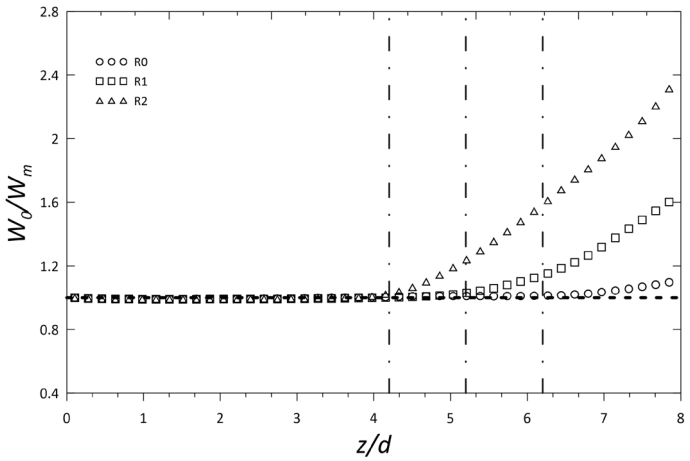

Fig. 6 Behavior of the mean axial velocity of the jet (W_m), normalized by the discharge velocity W_0, as a function of the vertical location z/d, in the range $0 < z/d < 8$ (i.e., jet development region). The extension of the potential core, $W_0/W_m = 1$ is clearly visible

where $M_0 = \pi x_0^2 \rho W_0^2$ is the jet momentum evaluated in the nozzle section. If the Reynolds number of the jet is large enough, we can write it as:

$$\frac{w_m}{\sqrt{M_0 \,/\, \rho z^2}} = C_1. \tag{13}$$

and, recalling the definition of M_0, we can obtain:

$$\frac{W_0}{w_m} = C_2 \left(\frac{z}{d}\right), \tag{14}$$

which indicates a linear decay of the normalized axial velocity with the distance from the nozzle. To assess the validity of previous predictions and to characterize the jet dynamics in more detail, we plot the behavior of the jet velocity evaluated on the jet axis, W_0/W_m, as a function of the normalized vertical distance from the nozzle, z/d. The results are shown in Fig. 6 (for the region near the jet nozzle, $0 < z/d < 8$) and in Fig. 7 (for the downstream region, $6 < z/d < 16$). Considering Fig. 6, we notice that W_0/W_m is initially constant for all three simulations, clearly indicating the presence of the potential core. However, the extension of the region where $W_0/W_m = 1$ is different for the different simulations. In particular, confirming results from the previous literature [10,39,40], we notice that the extension of the potential core is about $z/d = 6 \div 7$ for a free jet (see simulation R0), while it reduces to $z/d \sim 5$ for simulation R1 and to $z/d \sim 4$ for simulation R2.

The decay of the centerline jet velocity downstream of the potential core is shown in Fig. 7. Theoretical linear predictions (solid color lines) are also shown for comparison purposes. As appears, the decay of the centerline velocity is faster in the presence of surface waves compared to the stagnant case. In addition, the decay rate increases for increasing wave height (see the behavior of $R2$ compared to $R1$). Interestingly, while the centerline velocity behavior can be nicely parameterized as a linear function for R0 and R1 in the region $6 < z/d < 15$ (as also suggested by the theory), the situation becomes more complex for $R2$. In this case, the decay of the centerline velocity appears linear only between $6 < z/d < 13$, while it becomes superlinear at larger distances from the nozzle. This seems to agree with the parabolic behavior proposed by Barile et al. [29].

To quantify the spreading of the jet, in Fig. 8 we show the behavior of the normalized half jet width, b/d, as a function of the normalized vertical distance from the nozzle, z/d.

We clearly notice that the jet width increases with increasing distance from the nozzle, and the behavior is well approximated by a linear function $b/d \sim C\,(z/d)$. The slope C of the curve depends not only on the distance from the nozzle (with a smaller slope during the first stages of the jet development, and a larger slope further downstream), but also on the amplitude of the surface waves. In particular, the spreading of the jet, which in a quiescent fluid is mild ($b/d \sim 2$ at $z/d = 15$), increases remarkably in a wavy environment (reaching up to $b/d \sim 5$ at $z/d = 15$ for $R2$).

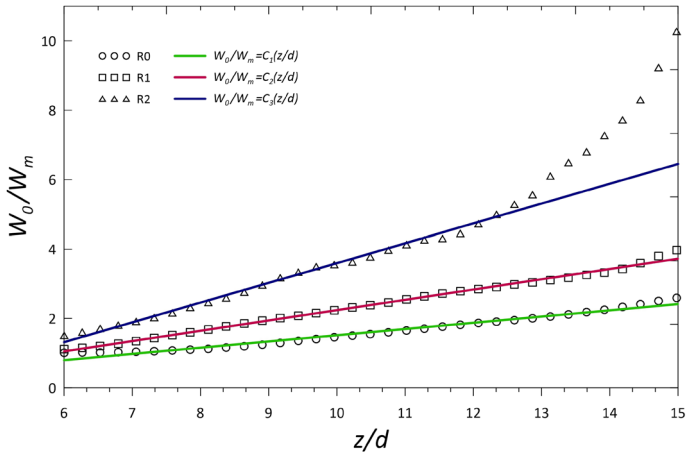

Fig. 7 Behavior of the mean axial velocity of the jet (W_m), normalized by the discharge velocity W_0, as a function of the vertical location z/d, in the range $6 < z/d < 15$ (i.e., developed flow region). Proposed linear scaling laws are also given: $C_1 = 0.175$, $C_2 = 0.298$ and $C_3 = 0.571$

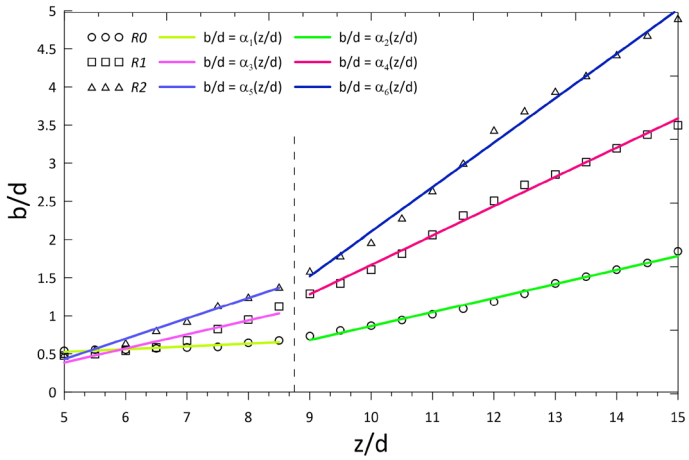

Fig. 8 Behavior of the normalized jet width (b/d), as a function of the vertical location z/d, in the range $5 < z/d < 15$ (i.e., developed flow region). Proposed linear scaling laws are also given: for $R0$, $\alpha_1 = 0.03$ and $\alpha_2 = 0.18$; for $R1$, $\alpha_3 = 0.15$ and $\alpha_4 = 0.38$; for $R2$, $\alpha_5 = 0.26$ and $\alpha_6 = 0.58$

3.5 Interactions between the submerged jet and the surface waves

To visualize the interaction between the jet and the surface waves, in Fig. 9a we show the structure of the flow on a longitudinal plane ($x - z$) for R0, R1 and R2. Velocity vectors on the $x - z$ plane (shown for a small portion of the domain, $1.5 < x < 2.5$) are shown together with a velocity contour map (red indicates positive velocity, and blue negative velocity). The comparison between the different cases highlights the influence of the waves on the development of the jet. In particular, for R0, we notice that the jet is almost symmetric and, upon impingement on the free surface, induces free surface deformation. For R1 and R2, the jet loses its symmetry, and it is deflected by the wave motion. In addition, the deformation of the interface is mainly due to the presence of waves, with the deformation induced by the jet playing only a minor role.

We now provide a more quantitative measure of the influence of the jet on the surface waves by computing the frequency spectrum of the surface deformation at $y = 0$ and at four different locations along the x direction: $x = 0$, $x = 0.05\ m$, $x = 0.1\ m$, $x = 0.15\ m$. The results are shown in Fig. 10 for $R0$ (Fig. 10a), $R1$ (Fig. 10b) and $R2$ (Fig. 10c). Together with the behavior of the frequency spectrum, in the insets of Fig. 10 we also show a close-up view of the qualitative behavior of the surface deformation. For the quiescent environment

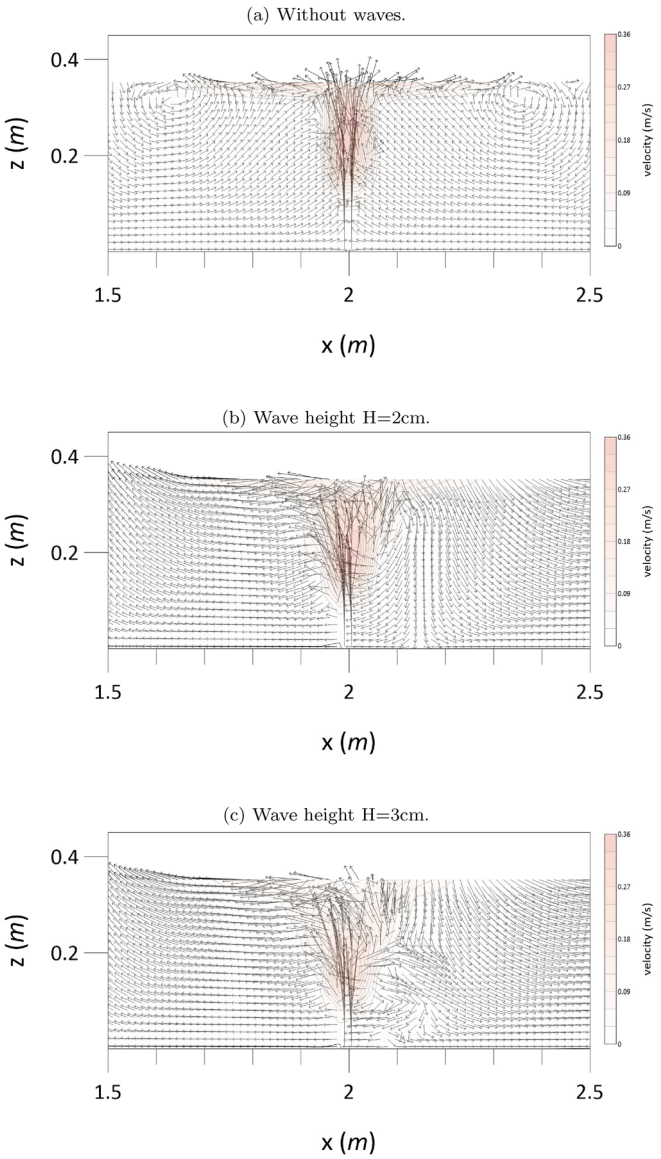

Fig. 9 Instantaneous vector velocity field on the cross sectional xz plane

(no imposed waves), we obtain a rather flat spectrum, which is the indication of a surface deformed by the vertical jet and showing no preferential deformation mode (as also confirmed by the qualitative picture in the inset of Fig. 10a). The situation is clearly different when the surface is characterized by imposed traveling waves (simulations $R0$ and $R1$). In this case, the spectrum displays a peak corresponding to the imposed wave frequency (1 Hz), along with other peaks at higher frequencies due to the propagation of jet-induced disturbances.

4 Conclusions

We have investigated the interaction between a vertical submerged jet, issued from a circular nozzle of diameter d located at the bottom of a horizontal liquid layer, and the top surface of the liquid layer, where mechanically generated waves propagate. By applying a phase-averaging technique, we decomposed the flow velocity and calculated the key flow statistics of the jet. Notably, we demonstrated that the potential core of the jet, where the axial velocity remains uniform and equal to the discharge velocity, contracts in the presence of surface

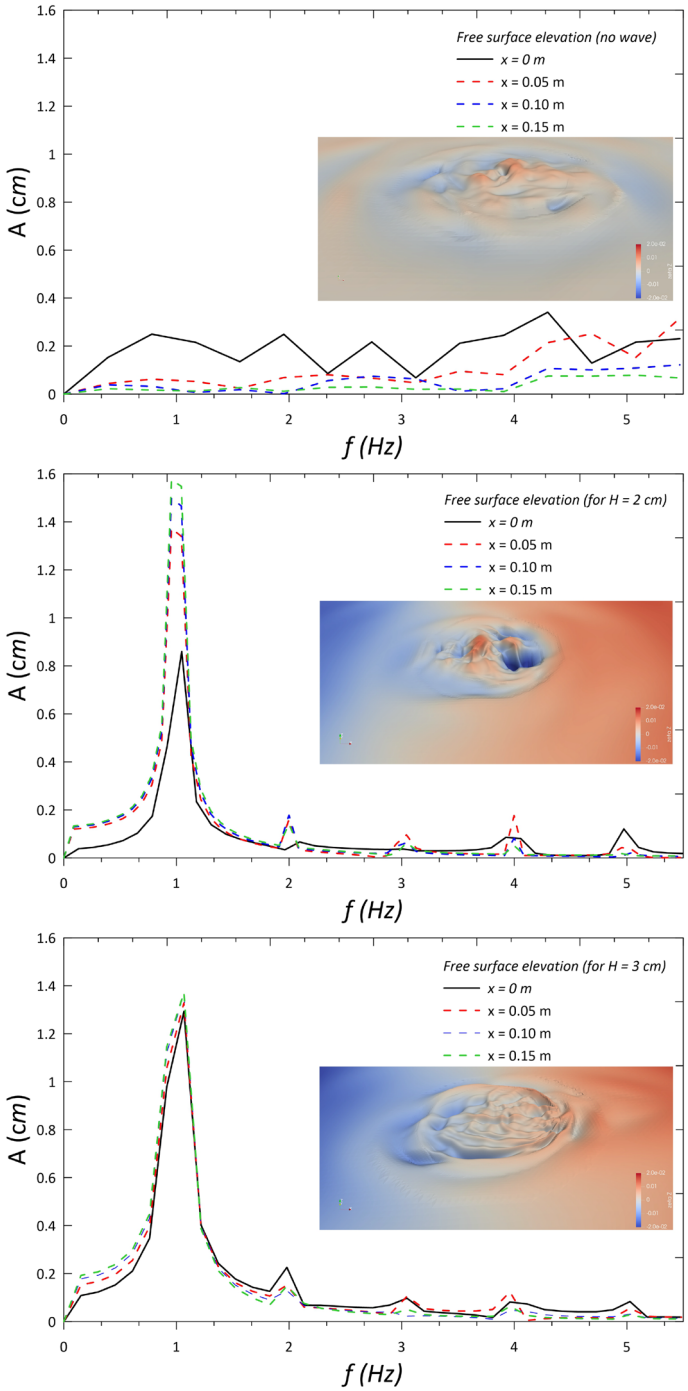

Fig. 10 Frequency spectrum of the free surface elevation for the three different cases considered in the present study: free surface (panel **a**); surface with traveling waves of amplitude $H = 2$cm and surface with traveling waves of amplitude $H = 3$cm. A snapshot of the instantaneous surface deformation for each case is given in the inset of each panel

waves. Specifically, the core length decreases from approximately $z/d \simeq 6$ in the absence of waves (case $R0$) to $z/d \simeq 4$ when waves of amplitude $H = 0.03$ m are present at the surface (case $R2$). Beyond the potential core, the axial jet velocity decays. For waves of small amplitude ($H \leq 0.02$ m, case $R1$), this decay is linear ($W_0/W_m \sim z$) with a slope influenced by the wave amplitude. However, for larger wave amplitudes ($H = 0.03$ m, case $R2$), the decay accelerates, becoming superlinear. As the jet develops downstream of the nozzle, its width increases linearly with distance, $b/d \sim C\,(z/d)$, with the C growth rate influenced by both the wave height and the distance from the nozzle. At an intermediate position along the jet axis, $z/d = 15$, we observed that the jet width expands significantly due to surface waves, increasing from $b/d \simeq 2$ in their absence (case $R0$) to $b/d \simeq 5$ for waves of amplitude $H = 0.03$ m (case $R2$). These findings underscore the profound impact of surface waves on jet dynamics, particularly in enhancing entrainment and dilution rates. Our results have significant implications for the protection of the environment and the design of hydraulic systems. The ability of surface waves to modulate jet behavior highlights their potential for improving mixing and dispersion in natural and engineered aquatic environments. These insights could inform the design of more effective hydraulic devices for applications such as pollutant dispersion, ultimately contributing to better environmental management and sustainable water resource engineering.

Software availability

Name of software: potentialFreeSurfaceFoam (OpenFOAM tool)
Developer: The OpenFOAM Foundation Ltd
Program language: C++
Cost: Free
Software availability: https://openfoam.org/.

Author contribution DM performed the numerical modeling; DM, DDP, MM and FZ analyzed the data; DM wrote the paper; DDP, MM, AS and FZ contributed suggestions, discussions, and reviewed the manuscript.

Funding Open access funding provided by Politecnico di Bari within the CRUI-CARE Agreement. No funding was received for conducting this study.

Declarations

Conflict of interest The authors have no relevant financial or non-financial interests to disclose.

Appendix A Mesh sensitivity analysis

A preliminary mesh sensitivity analysis has been performed to identify the resolution of the computational mesh that should be used to obtain reliable and robust results. To do that, we consider the reference case of a jet submerged in a stagnant liquid layer (i.e., corresponding to simulation R0 in the main body of the manuscript). The computational domain is the same used for the final simulations and is represented by a liquid layer of $4\,\text{m} \times 1\,\text{m} \times 0.35\,\text{m}$, with the jet nozzle in the center of the bottom boundary (see Sect. 2). Note that mesh refinement is applied on a truncated cone region corresponding to the jet development region (having a minor base diameter of 0.025 m near the jet nozzle and a major base diameter of 0.12 m near the free surface above the jet). Three different simulations are run corresponding to different values of the minimum base mesh size Δ (that is, the reference mesh size of the Cartesian mesh used to discretize the liquid layer) and of the minimum mesh size of the refined region Δ_r (which characterizes the truncated cone region). In particular, simulation-labeled LR is characterized by $\Delta = 0.01$ m and $\Delta_r = 6.25 \times 10^{-4}$ m (for an overall of approximately 9 million points); simulation-labeled MR is characterized by $\Delta = 0.005$ m and

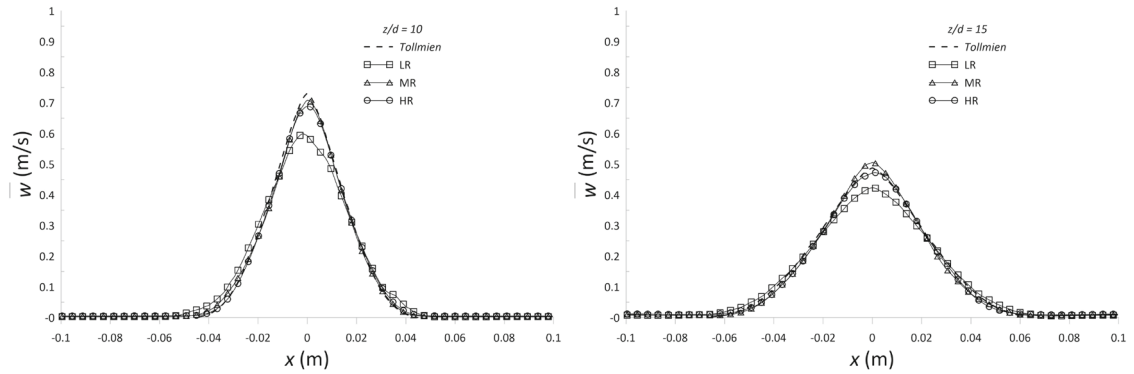

(a) $z/d = 10$ (b) $z/d = 15$

Fig. 11 Behavior of the mean jet velocity W at $z/d = 10$ (panel **a**), and $z/d = 15$ (panel **b**). Comparison between simulation LR (lower resolution, 9 grid points), simulation MR (medium resolution, 28 grid points) and simulation HR (higher resolution, 65 grid points). The theoretical prediction of Tollmien [34] is also given for comparison

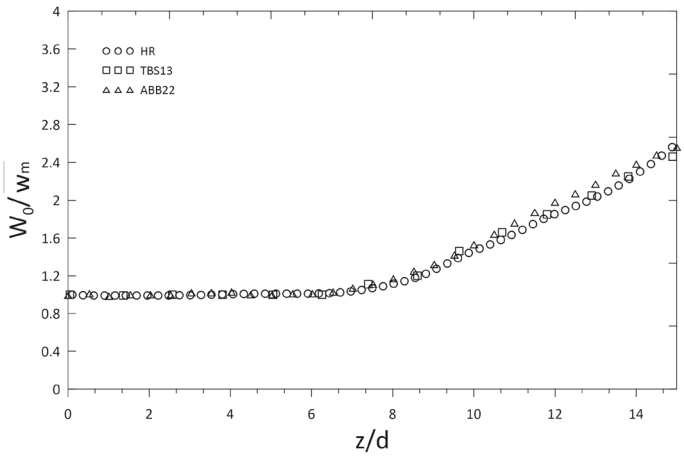

Fig. 12 Behavior of the ratio between the discharge velocity W_0 and the mean axial velocity of the jet (W_m), as a function of the vertical location z/d, in the range $0 < z/d < 15$ Comparison between current simulation (HR) and previous DNS data ([41], labeled TBS13, and [21], labeled ABB22)

$\Delta_r = 4.165 \times 10^{-4}$ m (for an overall of about 28 million points); simulation-labeled HR is characterized by $\Delta = 0.005$ m and $\Delta_r = 3.25 \times 10^{-4}$ m (for an overall of about 65 million points). The behavior of the mean jet velocity at two different locations, $z/d = 10$ and $z/d = 15$, is shown in Fig. 11a, b. The results of the numerical simulations are also compared with the theoretical solution of Tollmien [34]. We note that, while simulation LR underpredicts the jet velocity, simulations MR and HR provide good results, indicating that mesh convergence is achieved for the mesh resolution corresponding to MR. However, and for the sake of robustness, we decided to use the mesh resolution HR for the simulations presented in our manuscript.
To further benchmark our results, we have considered the behavior of the ratio between the discharge velocity, W_0 and the mean axial velocity of the jet, W_m, as a function of the vertical distance from the nozzle, z/d. The current results (case R0, without waves, mesh resolution HR) are compared with previous literature studies (DNS by [41], labeled TBS13 and [21], labeled ABB22). The comparison, which is given in Fig. 12, shows an overall satisfactory agreement.

Appendix B Turbulence statistics

The behavior of the normalized vertical and transverse normal stress and the shear Reynolds stress, $w'w'/W_0^2$, $u'u'/W_0^2$, and $u'w'/W_0^2$, respectively, are shown in Figs. 13 and 14 at three different locations, $z/d = 10$, $z/d = 12.5$ and $z/d = 15$. For better readability and without loss of generality, we show results only for the two limiting cases, R0 and R2. Confirming results from the previous literature [21,24,38], we observe that normal vertical stresses are typically larger than normal transverse and shear Reynolds stresses. We also notice the tendency of waves to broaden the jet width, as particularly visible in the behavior of the shear stress: the positive and negative peak of $u'w'/W_0^2$, which occur at the shear layer (i.e., at the jet boundary), are clearly pushed apart in simulation R2.

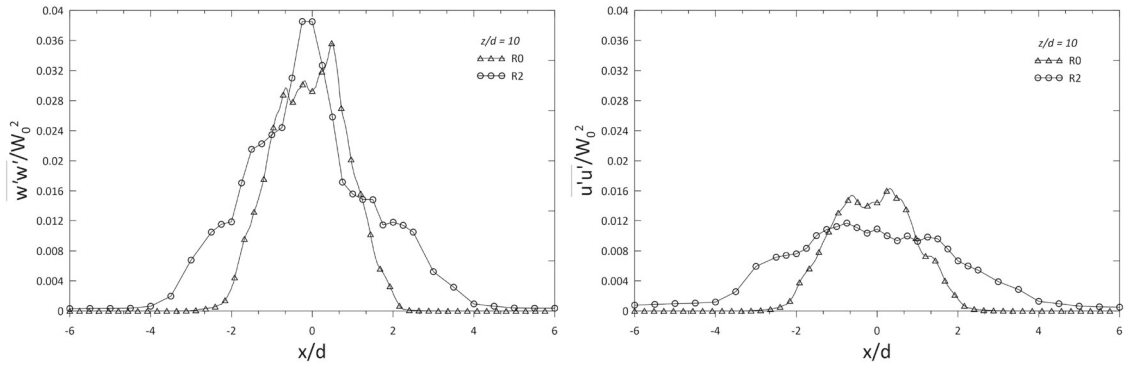

(a) Streamwise normal stress at z=0.2 m.

(b) Transverse normal stress at z=0.2 m.

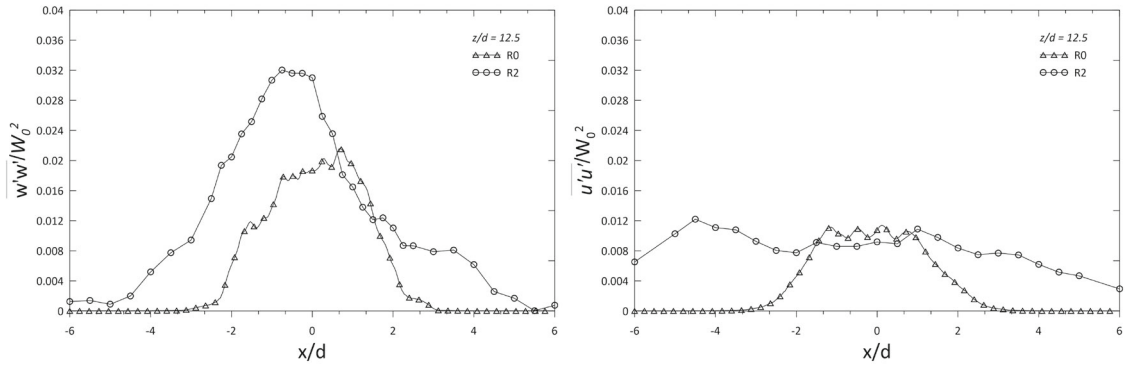

(c) Streamwise normal stress at z=0.25 m.

(d) Transverse normal stress at z=0.25 m.

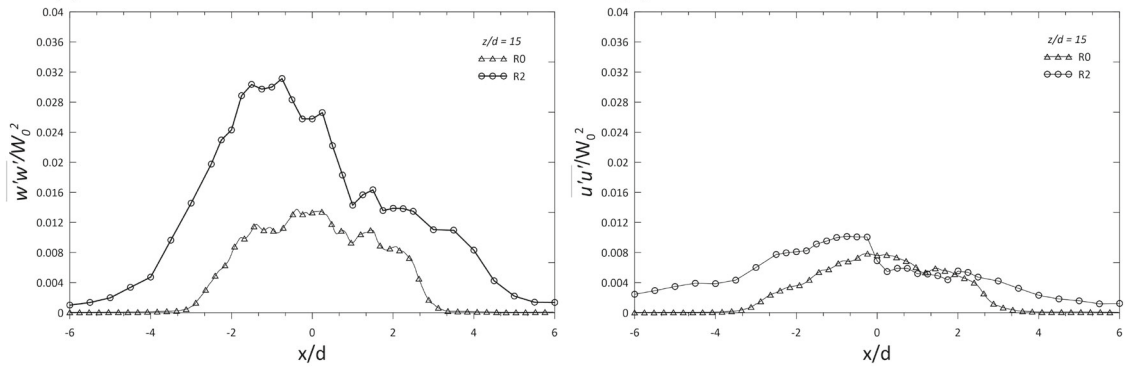

(e) Streamwise normal stress at z=0.3 m.

(f) Transverse normal stress at z=0.3 m.

Fig. 13 Behavior of the streamwise and transverse normal stress component

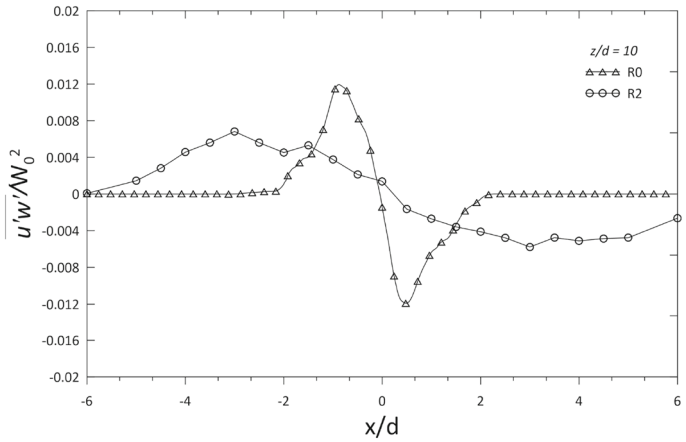

(a) Reynolds stress at z=0.2 m.

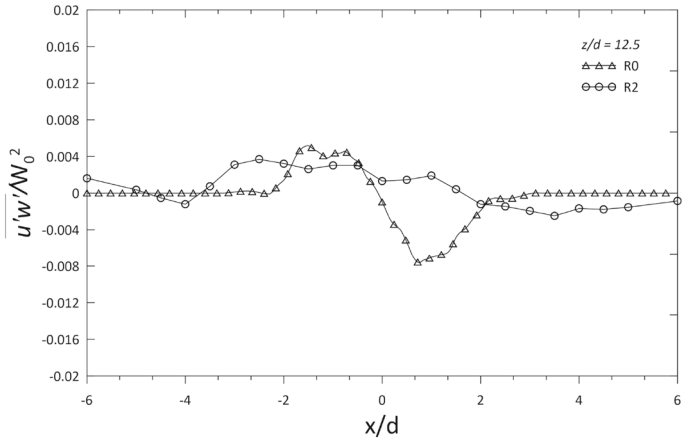

(b) Reynolds normal stress at z=0.25 m.

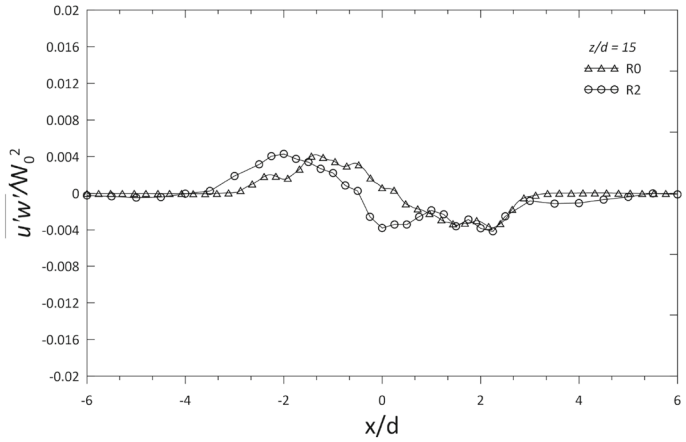

(c) Reynolds normal stress at z=0.3 m.

Fig. 14 Behavior of the shear Reynolds shear component

References

1. Blocken, B., Gualtieri, C.: Ten iterative steps for model development and evaluation applied to Computational Fluid Dynamics for Environmental Fluid Mechanics. Environ. Model. Softw. **33**, 1–22 (2012)
2. Roberts, P., Tian, X.: New experimental techniques for validation of marine discharge models. Environ. Model. Softw. **19**, 7–8 (2004)
3. Seung-Won, S.: NeA hybrid approach to particle tracking and Eulerian-Lagrangian models in the simulation of coastal dispersion. Environ. Model. Softw. **21**, 234–242 (2006)
4. Ali, K., Pateman, D.R.: Dispersion of marked fluid in reservoirs. Adv. Water Resour. **6**(4), 190–199 (1983)
5. Roberts, P.J., Salas, H.J., Reiff, F.M., Libhaber, M., Labbe, A., Thomson, J.C.: Marine Wastewater Outfalls and Treatment Systems. IWA publishing (2010)
6. Wygnanski Wygnanski, I., Fiedler, H.: Some measurements in the self-preserving jet. J. Fluid Mech. **38**(3), 577–612 (1969)
7. Ruochuan, G.: Numerical simulation of 2D buoyant jets in ice-covered and temperature-stratified water. Adv. Water Resour. **21**(5), 363–373 (1998)
8. Gohil, T.B., Saha, A.K., Muralidhar, K.: Numerical study of instability mechanisms in a circular jet at low Reynolds numbers. Comput. Fluids **64**, 1–18 (2012)
9. Anghan, C., Dave, S., Saincher, S., Banerjee, J.: Direct numerical simulation of transitional and turbulent round jets: evolution of vortical structures and turbulence budget. Phys. Fluids **31**(6), 065105 (2019)
10. Rajaratnam, N.: Turbulent Jets. Elsevier, Amsterdam (1976)
11. Fischer, H.B., List, E.J., Koh, R., Imberger, J., Brooks, N.H.: Mixing in Inland and Coastal Waters. Academic, New York (1979)
12. Wood, I.R., Bell, R.G., Wilkinson, D.L.: Ocean Disposal of Wastewater, Advanced Series on Ocean Engineering, vol. 8. World Scientific, River Edge, N.J. (1993)
13. Wen, Q., Kim, H.D., Liu, Y.Z., Kim, K.C.: Dynamic structures of a submerged jet interacting with a free surface. Exp. Thermal Fluid Sci. **57**, 396–406 (2014)
14. Chen, Y., Li, C., Zhang, C.: Numerical modeling of a round jet discharged into random waves. Ocean Eng. **35**(1), 77–89 (2008)
15. Shuto, N., Ti, L.H.: Wave effects on buoyant plumes. Coast. Eng. **1974**, 2199–2208 (1975)
16. Ger, A.: Wave effects on submerged buoyant jets. In: Proc., 8th Congress Int. Association for Hydraulic Research, pp. 295–300 (1979)
17. Sharp, J.J.: The effect of waves on buoyant jets. Proc. Inst. Civ. Eng. **81**(3), 471–475 (1986)
18. Chyan, J.-M., Hwung, H.-H.: On the interaction of a turbulent jet with waves. J. Hydraul. Res. **31**(6), 791–810 (1993)
19. Hwung, H.-H., Chyan, J.-M., Chang, C.-Y., Chen, Y.-F.: The diluition processes of alternative horizontal buoyant jets in wave motions. Coastal Eng. Proc. **1**(24) (1994)
20. Valero, D., Bung, D.B.: Sensitivity of turbulent Schmidt number and turbulence model to simulations of jets in crossflow. Environ. Model. Softw. **82**, 218–228 (2016)
21. Anghan, C., Bade, M.H., Banerjee, J.: Direct numerical simulation of turbulent round jet released in regular waves. Appl. Ocean Res. **125**, 103248 (2022)
22. Mori, N., Chang, K.A.: Experimental study of a horizontal jet in a wavy environment. J. Eng. Mech. **129**(10), 1149–1155 (2003)
23. Fang, S., Chen, Y., Xu, Z., Otoo, E., Lu, S.: An improved integral model for a non-buoyant turbulent jet in wave environment. Water **11**(4), 765 (2019)
24. Anghan, C., Bade, M.H., Banerjee, J.: A review on fundamental properties of the jet in the wave environment. Ocean Eng. **250**, 110914 (2022)
25. Kim, J., Choi, H.: Large eddy simulation of a circular jet: effect of inflow conditions on the near field. J. Fluid Mech. **620**, 383–411 (2009)
26. Gohil, T. B., Saha, A. K., Muralidhar, K.: Large eddy simulation of a free circular jet. J. Fluids Eng. **136**(5) (2014)
27. De Padova, D., Mossa, M., Sibilla, S.: Numerical investigation of the behaviour of jets in a wave environment. J. Hydraul. Res. **58**, 618–627 (2020)
28. De Padova, D., Mossa, M., Sibilla, S.: Characteristics of nonbuoyant jets in a wave environment investigated numerically by SPH. Environ. Fluid Mech. **20**, 189–202 (2020)
29. Barile, S., De Padova, D., Mossa, M., Sibilla, S.: Theoretical analysis and numerical simulations of turbulent jets in a wave environment. Phys. Fluids **32**(3), 035105 (2020)
30. Xu, Z., Chen, Y., Tao, J., Pan, Y., Zhang, C., Li, C.: Modelling of a non-buoyant vertical jet in waves and currents. J. Hydrodyn. Ser. B **28**(5), 778–793 (2016)
31. Ezhova, E., Cenedese, C., Brandt, L.: Interaction between a Vertical Turbulent Jet and a Thermocline. J. Phys. Oceanogr. **46**(11), 3415–3437 (2016)
32. Schmitt, P., Windt, C., Davidson, J., et al.: Beyond VoF: alternative OpenFOAM solvers for numerical wave tanks. J. Ocean Eng. Mar. Energy **6**, 277–292 (2020)
33. Kim, W.W., S. Menon, S.: A new dynamic one-equation subgrid-scale model for large eddy simulations. AIAA-95-0356(1995)
34. Tollmien, W.: Berechnung turbulente Ausbreitung-svorgane, ZAMM, Bd. 6, H. 6, S. 468-478, (1926)
35. Goertler, A.: Berechnung von Aufgaben der freien Turbulenz auf Grund eines neuen Näherungsansatzess. ZAMM, Bd. 22, H. 5, S. 244, (1942)
36. Wilmott, C.J.: On the validation of models. Phys. Geogr. **2**, 184–194 (1981)
37. Hussain, A., Reynolds, W.C.: The mechanics of an organized wave in turbulent shear flow. J. Fluid Mech. **41**(2), 241–258 (1970)
38. Mossa, M.: Behavior of nonbuoyant jets in a wave environment. J. Hydraul. Eng. **130**(7), 704–717 (2004)
39. Abramovich, G.N.: The Theory of Turbulent Jets. MIT Press, Cambridge, Mass (1963)

40. Hussein, H.J., Capp, S.P., George, W.K., et al.: Velocity measurements in a high-Reynolds-number, momentum-conserving, axisymmetric, turbulent jet. J. Fluid Mech. **258**(1), 31–75 (1994)
41. Taub, H., Lee, S., Balachandar, S.S.: A direct numerical simulation study of higher order statistics in a turbulent round jet. Phys. Fluids **25**(11) (2013)